ChemCatChem

Research Article
doi.org/10.1002/cctc.202401161

Chemistry Europe
European Chemical Societies Publishing

www.chemcatchem.org

Supramolecular Preorganization Rhodium and Iridium Metal Complexes Within $M_{12}L_{24}$ Self-Assembled Nanospheres for the Confined Synthesis Rh/Ir Alloyed Nanoparticles

Lotte L. Metz,[a] Eduard O. Bobylev,[a] Rim C. J. vandePoll,[b] Emiel J. M. Hensen,[b] Igor Hoogsteder,[c] Wiebke Albrecht,[c] and Joost N. H. Reek*[a]

Controlling the size and composition of metal nanoparticles is of considerable interest, as these are essential to their catalytic properties. Recently, our group has developed a preorganization strategy for controlled Ir nanoparticle synthesis inside $Pt_{12}L_{24}$ nanospheres. In the current contribution, we expand this method to the controlled synthesis of Rh nanoparticles. The encapsulated Rh^{I} complexes (**Rh-s @ G-sphere**) led to reasonable size control (2.8 ± 0.9 nm). Next, we demonstrated the formation of Rh-Ir alloyed nanoparticles with varying Rh/Ir compositions, by preorganization of the respective metal complexes inside $Pt_{12}L_{24}$ nanospheres based on complementary hydrogen bonds before the reduction step that leads to nanoparticle formation. These heterometallic particles were evaluated in the hydrogenation of cinnamaldehyde (**7**) as a probe reaction. Besides a high activity in this probe reaction, the Rh particles also catalyzed the conversion of the solvent (CH_3CN). The formed basic amine leads to follow-up reactions of the product and compatibility issues with the hosting nanosphere. The solvent hydrogenation was effectively suppressed by using the Rh:Ir alloyed nanoparticles, provided that they contain > 66% Ir. Compared to the monometallic Ir particles (**Ir-s @ G-sphere**), the Rh:Ir alloyed nanoparticles displayed higher catalytic activity, reaching optimal selectivity and activity at an 8:16–Rh:Ir ratio. The combined catalytic results illustrate that preorganization of the metal complexes in the nanosphere before the reduction with hydrogen effectively facilitates the formation of Rh:Ir alloyed nanoparticles, which allows for tuning a catalyst to create a more active and selective catalyst compared to monometallic or nonencapsulated Rh/Ir particles.

1. Introduction

Rh nanoparticles are a popular class of catalysts and are applied in numerous catalytic transformations, mostly for the hydrogenation of unsaturated organic substrates.[1–3] The unique properties of small nanoparticles have received ample attention in the field of catalysis, owing to their high surface-to-volume ratio, commonly robust character, and tuneable features.[4–6] It is by now widely accepted that the unique characteristics of these nanoparticles are governed by their precise dimensions, composition, and surface environment. Hence, gaining control over these properties to tune their catalytic features is key and developing synthetic methods for the controlled preparation of nanoparticles is of substantial interest.[7,8]

In the past decades, various synthetic strategies have been reported aiming to gain control over the properties of these nanoparticles. These include microheterogeneous systems, such as polymers,[9–11] biphasic systems,[12,13] dendrimers,[14–16] and discrete porous materials.[17–21] In general, these methods rely on the spatial separation of the formed nuclei from the bulk thereby controlling further growth modes.[22–27] The dimensions and local metal precursor concentration within these microenvironments strongly influence the resulting particle size and distribution.[22] Thus, creating a well-defined cavity with a high level of control over its contents is of considerable interest.

Recently, our group has developed a method for catalyst encapsulation within well-defined guanidinium functionalized $M_{12}L_{24}$ coordination spheres (M = Pd or Pt, **G-sphere**, Figure 1).[28–36] In addition, we have demonstrated that these self-assembled coordination spheres (**G-sphere**) can also be applied as well-defined nanoreactors for the controlled synthesis of ultrafine **Ir** nanoclusters (1.8 ± 0.4 nm).[37] These encouraging results led us to explore if this new methodology could be applied in the templated nanoparticle synthesis, in which metal complexes are preorganized before the reduction, with other catalytically relevant metals such as Rh.

In this work, we describe the preorganization and hydrogenation of sulfonate-bearing NHC-based Rh^{I} complexes (**Rh-s**)

[a] Dr. L. L. Metz, Dr. E. O. Bobylev, Prof. Dr. J. N. H. Reek
van 't Hoff Institute for Molecular Science, University of Amsterdam, Amsterdam 1098XH, The Netherlands
E-mail: J.N.H.Reek@uva.nl

[b] R. C. J. vandePoll, E. J. M. Hensen
Department of Chemical Engineering and Chemistry, Eindhoven University of Technology, Eindhoven 5600MB, The Netherlands

[c] I. Hoogsteder, W. Albrecht
Center for Nanophotonics, NWO Institute AMOLF, Amsterdam 1098XG, The Netherlands

Supporting information for this article is available on the WWW under https://doi.org/10.1002/cctc.202401161

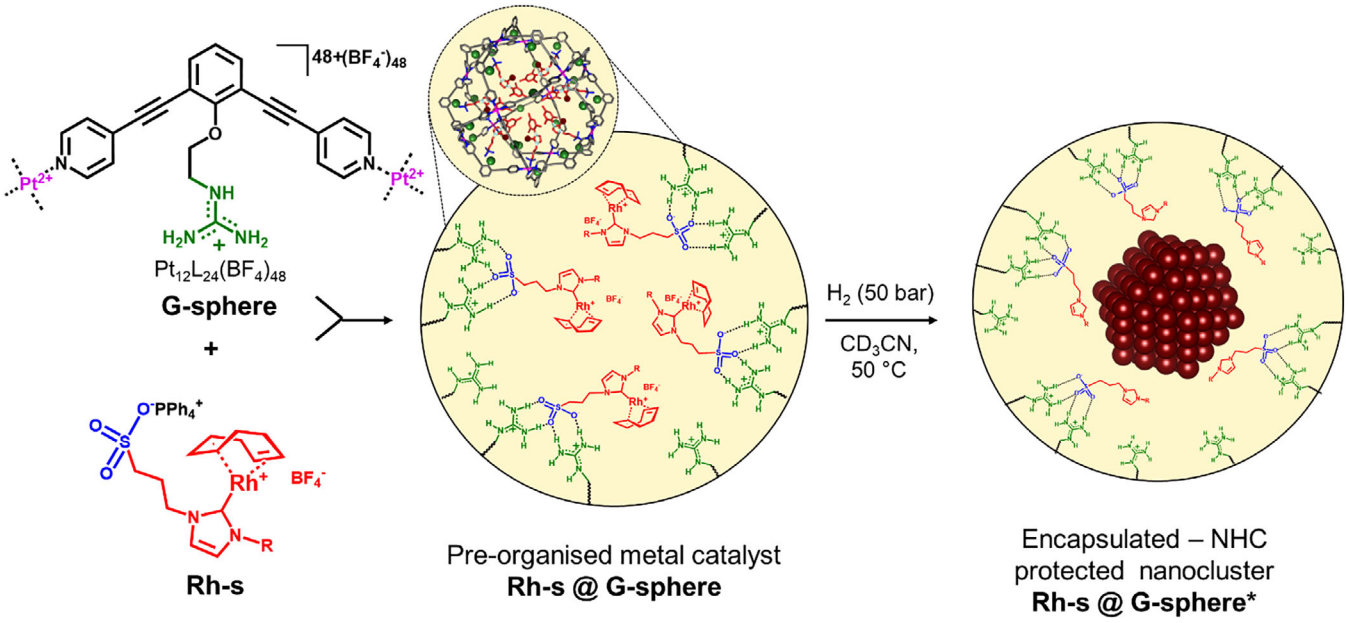

Figure 1. Schematic representation of the preorganization strategy for the controlled synthesis of encapsulated Rh-NPs.

within well-defined [$Pt_{12}L_{24}$] nanospheres (**G-sphere**). Reduction of these preorganized metal complexes (**Rh-s @ G- sphere**) resulted in the formation of small Rh nanoparticles (average diameter 2.8 ± 0.9 nm), which were found to be catalytically active in the hydrogenation of cinnamaldehyde. The nanoparticles were so reactive that also the solvent (CH_3CN) was converted and the formed amine product led to compatibility issues with the nanosphere as it slowly decomposed. Rh:Ir alloyed particles were also prepared through preorganization of Rh^I and Ir^I complexes (**Rh-s** and **Ir-s**) in varying ratios and subsequent reduction. This new manner to make alloyed nanoparticles resulted in systems that were no longer reducing the solvent. We demonstrate a new strategy to form Ir-Rh alloyed nanoparticles, which has a strong the impact on the catalytic activity of the nanoparticle in reductive catalysis.

2. Results and Discussion

2.1. Strategy

The strategy outlined in Figure 1 involves the preorganization of 24 sulfonated metal complexes in a well-defined $M_{12}L_{24}$ nanosphere, bearing 24 guanidinium binding sites. Hydrogenation of the preorganized metal complexes leads to the templated formation of nanoclusters. The metal precursor (**Rh-s**) was chosen based on three specific requirements: The metal complex should be 1) stable and remain strongly bound to the sulfonate-bearing ligand during encapsulation, 2) readily and cleanly be converted to nanoparticles upon hydrogenation and 3) function as a stabilizing ligand for the resulting nanocluster. We anticipated that an *N*-heterocyclic carbene-based (NHC) metal complex like **Rh-s** would embody these requirements.[38–40]

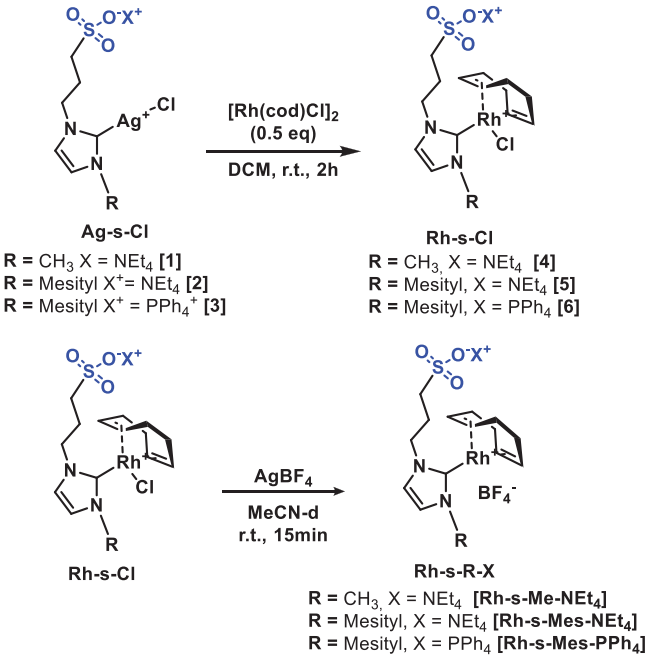

Scheme 1. Synthesis of sulfonate functionalized NHC-based Rh^I complexes (**Rh-s-R-X**).

2.2. Synthesis of the G-Sphere and the Guest Complexes

The [$M_{12}L_{24}$] coordination nanospheres (M = Pt^{II} or Pd^{II}, **Pt-G-sphere**, and **Pd-G-sphere,** respectively) were prepared and characterized as previously reported.[35,37,41]

Several sulfonate functionalized NHC-based Rh^I complexes were synthesized via a modified literature procedure through transmetallation of the corresponding silver carbene (**Ag-s-Cl**, Scheme 1).[42] In the final step, the chloride counter ion was exchanged with BF_4^- to prevent possible compatibility issues

of the chloride ions with the $[Pt_{12}L_{24}]$ coordination sphere. To study the influence of ligand substituents on particle formation, the N-functional group of the NHC was also varied (Scheme 1, R=**CH_3** or mesityl (**Mes**)). It should be noted that in initial experiments the system was studied with **Rh-s** complexes bearing a tetraethyl ammonium (**NEt_4^+**) counterion. This counterion was later replaced by tetraphenylphosphonium (**PPh_4^+**) for practical reasons which will be discussed in a later section (vide infra). All complexes described in this work were obtained through the similar synthetic procedure in comparable yields and were characterized by ^{1}H-NMR, ^{13}C-NMR, and mass spectrometry (MS). Notably, the methyl-functionalized **Rh-s** complex (**Rh-s-Me**) displayed a lower stability compared to the mesityl-functionalized metal complexes (**Rh-s-Mes**).

2.3. Encapsulation of the Rh-s Metal Complex

Endohedral binding of **Rh-s** inside the nanosphere (**G-sphere**) was demonstrated by ^{1}H-NMR, ^{1}H-DOSY-NMR, and cold-spray-ionization time-of-flight mass spectrometry CSI-TOF-MS experiments. The results of these studies will be discussed in the following section.

To gain insight into the host-guest interaction of **Rh-s** and the encapsulation capacity of the host (**G-sphere**), metal complex encapsulation within the nanosphere was established by a titration experiment monitored by ^{1}H-NMR (Figure 2). Host-guest interactions are indicated by the strong shifts in the NH signal of the guanidinium functionality (Figure 2). Notably, the other signals of the sphere (Figure 2) remain relatively unchanged, suggesting that the guest primarily interacts with the guanidinium functionality inside the sphere. To study the encapsulation capacity of the host, the guanidinium NH shifts, resulting from sulfonate binding, are plotted as a function of the number of Rh guest (**Rh-Me-NEt_4^+**) equivalents added to the nanosphere (**G-sphere**) (Figure 2). Initially, the shift follows a steep linear trend with increasing guest concentration ([**Rh-Me-NEt_4^+**]) but abruptly ceases upon approaching the maximum number of binding sites within the sphere (24 equiv.). Notably, the observed N-H-shift difference starts to deviate from this linear trend after 20 equiv., indicating weaker binding of the final four guest molecules. These results are in line with previously reported observations for the analogous Ir^I complex.[37] Overall, these results demonstrate the endohedral interaction and anticipated encapsulation capacity of the sphere.

Guest encapsulation was further confirmed by ^{1}H-DOSY-NMR (Figures S14–S16). The observed diffusion coefficients of the guest complex (**Rh-s**) in the presence of the sphere (**Rh-s @ G-sphere**, LogD $= -9.49$ m^2s^{-1}) are close to those observed for the empty sphere (LogD $= -9.59$ m^2s^{-1}), suggesting that the metal complex is encapsulated.

Finally, formation of the host-guest complex (**Rh-s @ G-sphere**) was confirmed by CSI-TOF-MS spectra of a solution of the nanosphere in the presence of four equivalents of **Rh-s-Me-NEt_4**, which displayed multiply charged species that can be assigned to the nanosphere hosting different numbers of **Rh-s** complexes, ranging from 1–6 equivalents of **Rh-s** per nanosphere (Figures 2c, S20–S22 and Table S2). The same experiment with two equivalents of **Rh-s-Me-NEt_4** provides similar results but displays species in the range of 0–4 equivalents of **Rh-s** guest complex per **G-sphere**. It should be noted that for experiments with increasing guest concentrations (8, 16, or 20 eq **Rh-s** vs. **G-sphere**), the number of possible host-guest complex combinations increases, leading to broader peaks in the resulting mass spectra (Figure 2d and Table S3). Overall, these experiments combined clearly confirm the strong interaction of these sulfonate-functionalized metal complexes with the sphere. Satisfyingly, the binding studies of **Rh-s** display similar to identical results compared to the previously reported related Ir^I complexes (**Ir-s**)[37] and underline the generality of the strategy. Having established that up to 24 Rh^I metal complexes can be bound inside the sphere, we set out to explore the effects of encapsulation on controlled nanoparticle formation.

2.4. Rh Nanoparticle Synthesis and Characterization

To establish if nanoparticles can be prepared within the nanospheres, the **Rh-s-NEt_4** metal complexes were hydrogenated either in the presence or absence of the sphere. The particles were prepared by hydrogenation of a 24:1 mixture of **Rh-s-NEt_4** and **G-sphere**, (1 ml, 8.7 mM, and **Rh-s @ G-sphere**) and the CD_3CN solution was kept at 50 bar H_2 and 50 °C for 16 h to allow full reduction of the metal complexes (Figure 3). After 16 h of reaction time, hydrogenation of **Rh-s-Me-NEt_4** (**R = CH_3**) in the presence of the sphere (**G-sphere**) led to the formation of a deep red solution, with a dark precipitate on the wall of the vial (Figure S23). In contrast, the hydrogenation of the metal complex in absence of the sphere led to the formation of a colorless solution and a dark film, indicative of the formation of bulk Rh which is no longer in solution. Although the difference in these results demonstrates an encouraging encapsulation effect, the encapsulated particles display precipitate formation, indicative of either decomposition or aggregation. Therefore, the templated synthesis was further explored with the related mesityl functionalized analog: **Rh-s-Mes-NEt_4** (R = **Mes**) (Figure 3). Hydrogenation of **Rh-s-Mes-NEt_4** (R = **Mes**) in the presence of the nanosphere (**Rh-s @ G-sphere**) resulted in the transformation of an orange homogeneous solution to a deep red-brown solution without the formation of any precipitate, indicating all Rh was still in solution and no agglomeration had occurred (Figure 3).

Similar to the related methyl complex (**Rh-Me-NEt_4**), hydrogenation of the free metal complex (**Rh-Mes-NEt_4**) in the absence of the sphere under identical conditions resulted in the formation of a clear solution and a grey mirror film, indicating agglomeration and consequent formation of a bulk-metal film. These contrasting results illustrate the protective effect of encapsulation during nanoparticle synthesis. Unfortunately, although initially a homogeneous **Rh-s @ G-sphere*** solution was obtained, gradual formation of precipitate was observed within a week, indicative of system degradation and/or particle agglomeration.

As a control, nonencapsulated nanosphere-metal complex combinations were prepared and hydrogenated. For these con-

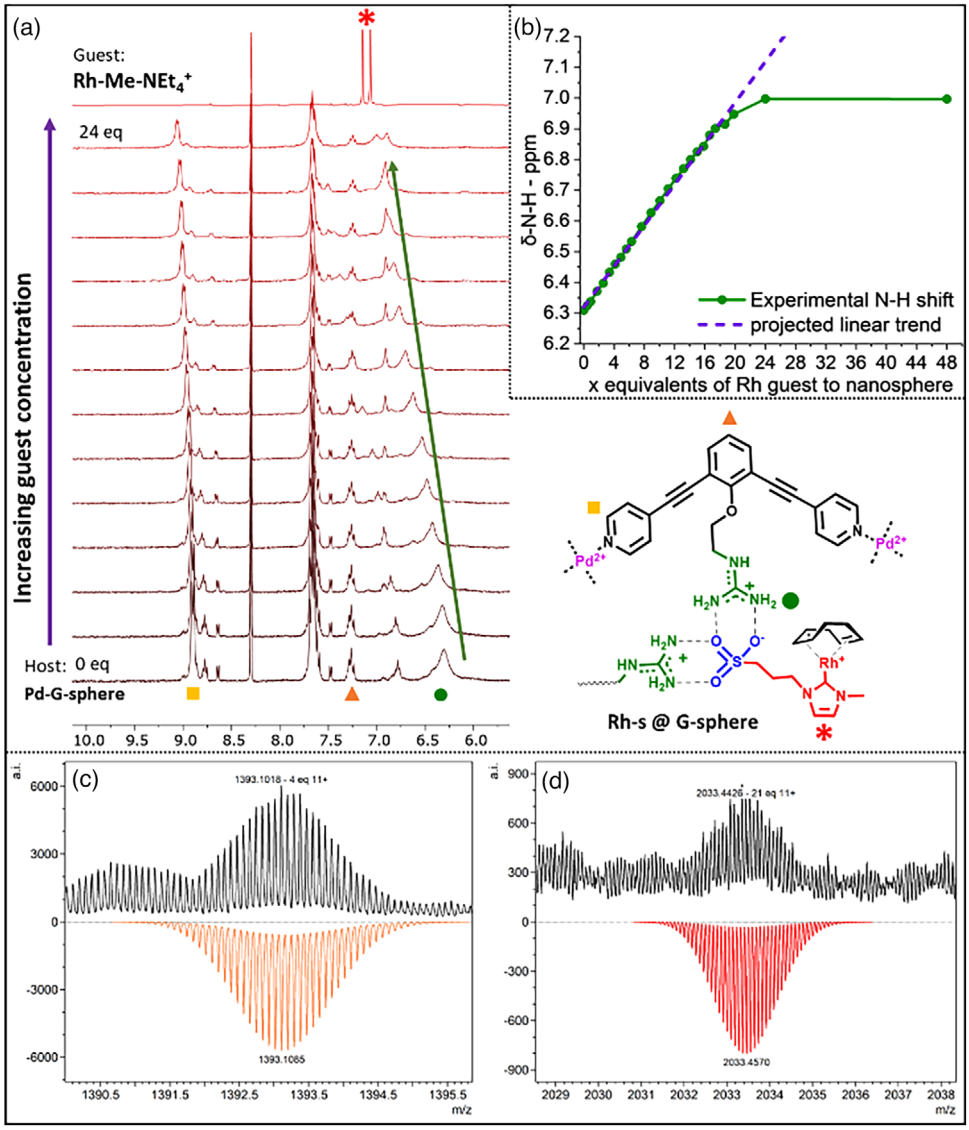

Figure 2. (a) Stacked ^{1}H-NMR spectra of an encapsulation titration experiment and (b) N-H shift plotted against the number of equivalents of Rh-guest (**Rh-Me-NEt$_4$**$^+$) added with respect to the sphere (**Pd-G-sphere**). **Bottom**: Zoom of CSI-TOF mass spectra of the **Pd-G-sphere** with (c) 4 equiv. **Rh-s** added (4 equiv. highest signal) or (d) 20 equiv. **Rh-s** added (21 equiv. highest signal), with a spray temperature of −40 °C and a dry gas temperature of −35 °C, with the simulated spectra in color.

trol groups, either the sulfonate binding moiety or the guanidinium functionality of the nanosphere was replaced with an aliphatic group (**Rh-p** and **M-sphere**, Figures S17–S18). The lack of encapsulation for these control groups (**Rh-p + G-sphere** and **Rh-s + M-sphere**) was established by ^{1}H-DOSY-NMR (Figures S17–S18). Hydrogenation of the solutions of both control groups led to the formation of dark suspensions (Figure S25). These results further underline the role of encapsulation in controlled nanoparticle formation.

Overall, the perceived impact of encapsulation is similar to observations of the previously described templated Ir nanocluster formation.[37] However, in contrast to the analogous Ir-system, the solution containing **Rh-s @ G-sphere*** displays gradual precipitate formation within a week, whereas the previously reported Ir nanoclusters remain homogeneous far beyond this timespan (months).

To evaluate these differences in more detail, the **Rh-s @ G-sphere*** particles were characterized by transmission electron microscopy (TEM) (Figure 3b). The samples for these measurements were prepared directly after hydrogenation without further purification. The TEM images of the encapsulated Rh nanoparticles (**Rh-s @ G-sphere***) reveal particles with an average diameter of 2.8 ± 0.9 nm (Figure S24). These dimensions are relatively large compared to their related encapsulated Ir nanoclusters (1.8 ± 0.4).[37] The majority of the measured particles are smaller than the dimensions of the sphere (5 nm).[43] However, particles with a larger diameter were also identified, indicating that some particles may no longer be confined within the sphere. Furthermore, the TEM images displayed in Figure 3b indicate that the **Rh-s @ G-sphere*** particles on the grid are surrounded by a sizeable amount of residual material, visible from the grey area surrounding the clusters. This residual material

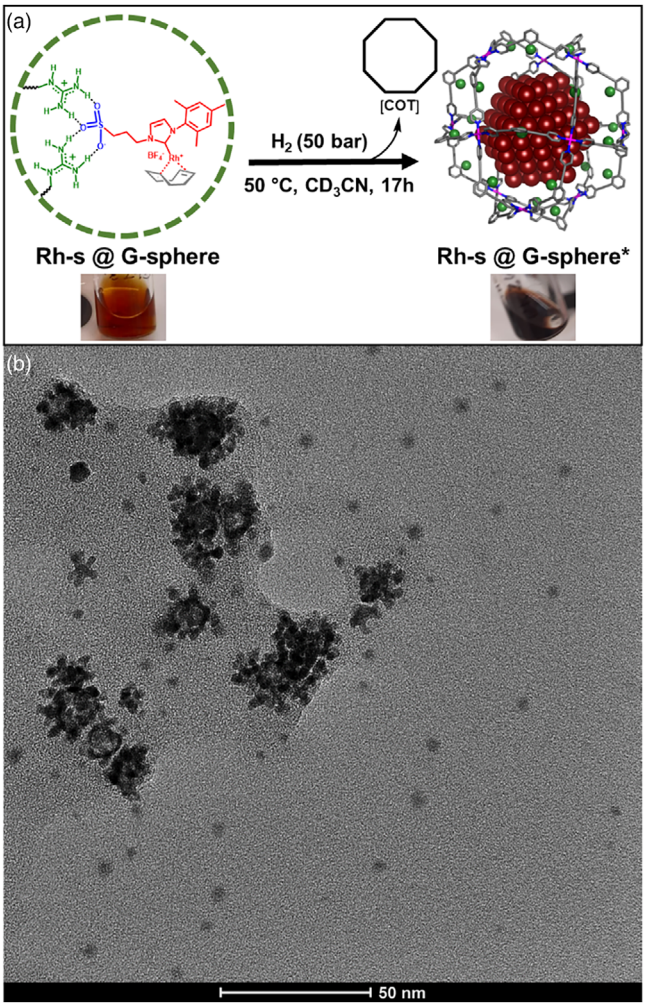

Figure 3. Nanoparticle synthesis with encapsulated **Rh-s-Mes-NEt$_4$** with (a) synthesis conditions and representative images of the solutions of **Rh-s @ G-sphere** before and after hydrogenation (**Rh-s @ G-sphere***) respectively. (b) Representative TEM image of **Rh-s @ G-sphere***.

could be the result of incomplete evaporation of organic materials, which generally includes high boiling solvents or excess ligand. When considering the identical preparation methods used for the Ir and Rh particles and their TEM samples, the presence of such excess material may be an indication of the formation of some unexpected products. Furthermore, the nature of these products may also shed light on the observed size and gradual precipitation over time. To investigate this, the product composition after hydrogenation was examined by ^{1}H-NMR spectroscopy.

The ^{1}H-NMR spectra of a solution **Rh-s-Mes-NEt$_4$ @ G-sphere** or **Rh-s-Mes-NEt$_4$** after hydrogenation (Figure S26) reveal the loss of the characteristic **Rh-s** signals, accompanied by the formation of the imidazolium salt and display complete hydrogenation of the cyclooctadiene ligand (COD) to cyclooctane (**COT**, 1.54 ppm), suggesting the complete conversion of the **Rh-s** complex. Notably, the characteristic signals of the nanosphere are absent, indicating that the nanosphere may have (partially) decomposed or is no longer in solution. Furthermore, aside from the expected signals, two additional prominent peaks have formed at 2.55 and 1.03 ppm (Figure S29), which appear to correspond to a mixture of ethyl-, diethyl- and triethylamine species. Initially, it was hypothesized that these side products were formed through the decomposition of the tetra-ethyl ammonium counterion (**NEt$_4^+$**). However, when the counterion was replaced by tetraphenylphosphonium (**PPh$_4^+$**), the formation of the same products was observed after hydrogenation of the complex (**Rh-s-Mes-PPh$_4$,** Figure S28). As it was not the decomposition of the counterion, these side products were proposed to originate from the solvent (CD_3CN). Indeed, the observed amines are products and intermediates of CD_3CN hydrogenation (Scheme S1[44,45]) and H/D exchange, catalyzed by the very reactive rhodium nanoparticles.[46]

Unfortunately, the formation of these primary and secondary amines is detrimental to the nanospheres' integrity, as the amines can coordinate to the Pt cornerstones of the nanosphere, leading to partial disassembly of its 3-D structure, in line with the observed gradual precipitation and disappearance of the sphere's ^{1}H-NMR signals (Figure S28). Sphere disassembly results in less protected nanoparticles which lead to particle agglomeration, in line with the experimentally observed larger particle dimensions for this system.

To mitigate uncontrolled solvent hydrogenation, alternative solvents were explored for the preparation of encapsulated Rh nanoparticles. To change to a different solvent system, the **Rh-s @ G-sphere** host-guest complex was isolated through precipitation and tested in a variety of solvents (Table S5), however only DMF and DMSO dissolved the **Rh-s @ G-sphere** precipitate. These solvents were subsequently used for nanoparticle formation under the hydrogenative conditions described earlier in the presence of the **Rh-p** complex (Figure S30). Remarkably, the newly formed Rh particles had proven themselves to be effective catalysts for the hydrogenation of both DMF and DMSO as well, which was immediately noticeable from the distinct smell emanating from the resulting reaction mixtures. The anticipated reaction products were later confirmed by ^{13}C-NMR to be NMe_3 and SMe_2 (originating from DMF and DMSO, respectively, Figures S31–S32). Markedly, the hydrogenation of the free complex in DMSO led to the formation of a dark colloidal mixture as opposed to the generally observed grey film (Figure S30), suggesting limited NP agglomeration. It can be argued that the SMe_2 product can coordinate to the NP surface and consequently provides a protective layer against further particle agglomeration. Overall, these side reactions are undesired, and their products are incompatible with the nanosphere. Therefore, also these solvents cannot be considered as a suitable alternative medium for templated Rh nanocluster synthesis.

In contrast to the **Rh** nanoparticles, the **Ir** nanoclusters described in our previous work do not display measurable catalytic activity for nitrile hydrogenation.[37] Considering this notion, we were curious if in the presence of **Ir** we can generate **Rh/Ir** alloyed particles and if the activity of these nanoparticles could be tamed to minimize solvent activation. In other words: can **Rh/Ir** alloyed particles at a certain composition be tuned to achieve specific substrate selectivity over the solvent? And can preorganization facilitate (enhanced) alloying of these metals?

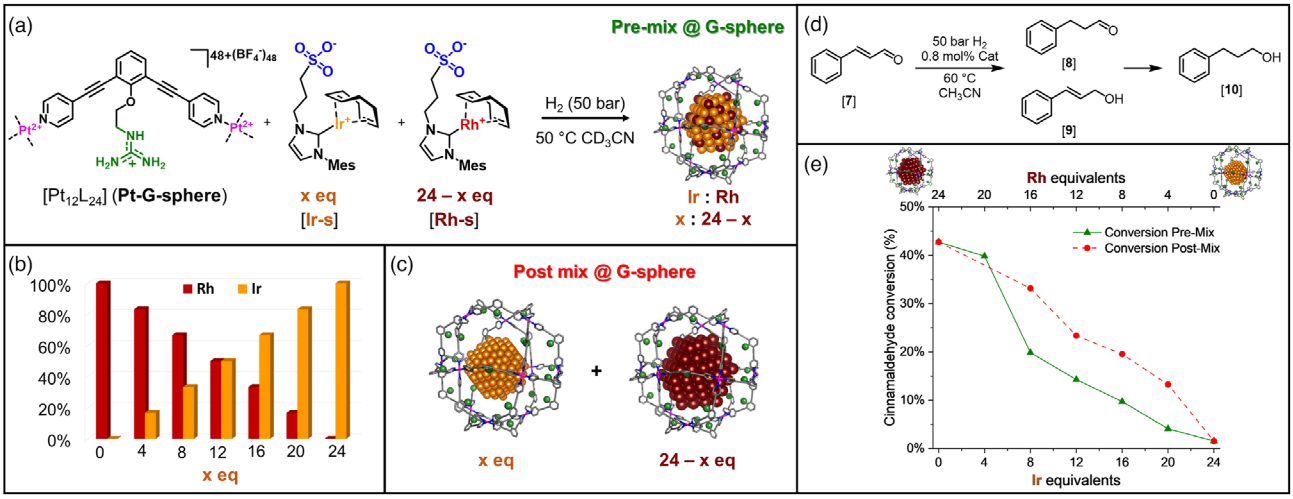

Figure 4. (a) and (b) Schematic representation of encapsulated mixing strategy (**Premix @ G-sphere**) and (c) the postmix control group (**Postmix @ G-sphere**). (d) Reaction conditions and potential products of cinnamaldehyde (**7**) hydrogenation. (e) Conversion of cinnamaldehyde (**7**) after 2 h in the presence of premixed and postmixed encapsulated nanoparticles. [7] = 0.42 M and 0.8 mol% catalyst versus **7** in CH_3CN (0.478 ml).

2.5. Alloying and Catalysis

To explore these questions, encapsulated nanoparticles with varying **Rh/Ir** compositions were prepared (**Premix G-sphere**, Figure 4a,b) and evaluated with cinnamaldehyde (**7**) hydrogenation as a model reaction (Figure 4d). As discussed in the previous section, amine formation is not observed in the presence of the **Ir** nanoclusters. It is therefore expected that the catalytic activity for converting the solvent will decrease with increasing **Ir** content. To compare the catalytic behavior of alloyed and nonalloyed encapsulated nanoparticles, a control group was devised (Figure 4c). In this control group, monometallic encapsulated nanoparticles of **Rh** and **Ir** were prepared separately and subsequently mixed after particle synthesis (**Postmix G-sphere**, Figure 4c). Both the premixed and postmixed particle solutions were prepared with the same Rh/Ir metal ratios and applied in catalytic experiments. It is hypothesized that alloyed **Ir/Rh** particles would display unique catalytic features compared to mixtures of their pure metal counterparts. Therefore, a linear correlation between the **Rh:Ir** ratio and solvent activation is expected in the presence of the postmixed nanoparticles, whereas in the case of effective alloying a nonlinear response is more likely.

The extent of alloying and its effect on selectivity was indirectly evaluated by the hydrogenation of cinnamaldehyde as a test reaction (Figure 4d). Cinnamaldehyde (**7**) can be hydrogenated at either the C=C or C=O bond to form hydrocinnamaldehyde (**8**) or cinnamyl alcohol (**9**), which could both be further reduced to form phenylpropanol (**10**). The conversion of cinnamaldehyde and product composition were evaluated by GC analysis in the presence of an internal standard.

In Figure 4e the conversion of **7** after 2 h is plotted as a function of the relative number of **Rh-s** and **Ir-s** equivalents with respect to the nanospheres. For the **Rh-s** and **Ir-s** @ **G-sphere** particles that are mixed after the formation, a linear decrease with increasing **Ir-s** content is observed, suggesting that no significant alloying takes place under catalytic conditions. In contrast, the **premixed** @ **G-sphere** particles display a sizable drop in activity starting from a Rh:Ir ratio of 16:8, and does not follow the same direct correlation as found for the **postmixed** @ **G-sphere** particles, suggesting that under these conditions Rh-Ir alloyed nanoparticles were formed.

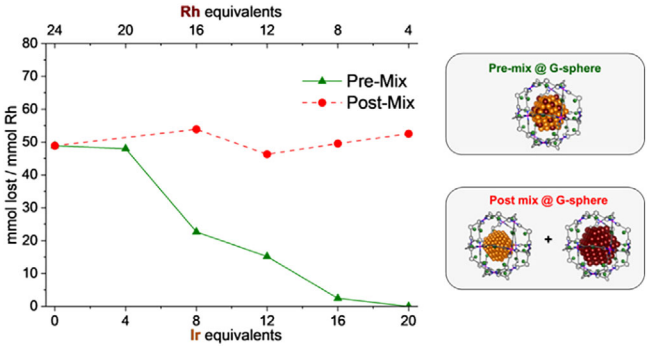

Figure 5. Mass balance discrepancy for the hydrogenation of [**7**] in relation to the catalyst composition, expressed as mmol material lost divided by Rh (mmol) as a function of the relative Rh:Ir ratio in the catalyst. (After 2 h in the presence of **Premixed** and **Postmixed** encapsulated nanoparticles. [**7**] = 0.42 M and 0.8 mol% catalyst vs. **7** in CH_3CN (0.478 ml).

Next, the product composition was evaluated (Figure S33), and hydrocinnamaldehyde (**8**) was identified as the major product. Notably, the amount of product formed (mmol **8** = 2–20 µmol) does not match the amount of substrate **7** converted (3–90 µmol) in most cases. In other words, based on the expected products, a sizable mass balance discrepancy is observed, varying from 0–40% depending on the Rh:Ir ratio and degree of metal mixing (Figure S34). This mass balance discrepancy was further investigated and a few of the major side products were identified by means of GC-MS analysis. Examination of the product composition revealed the presence of products that were formed by intermolecular aldol condensation of **8** (Scheme S2). Furthermore, amine species originating from solvent hydrogenation are suspected to react with **7** and **8** to form condensation products (Scheme S2). The variety of these condensate

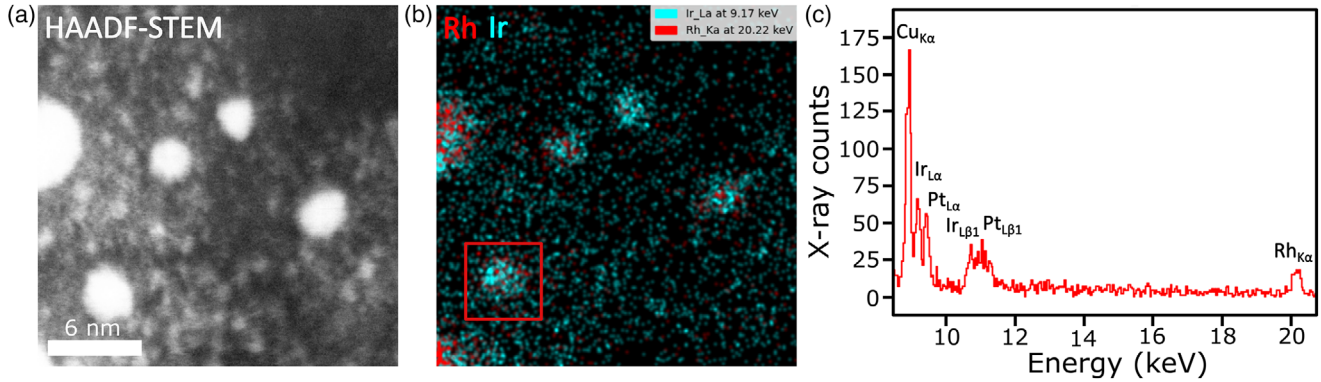

Figure 6. (a) HAADF-STEM image of **Premix @ G-sphere*** (Rh:Ir = 1:1) and (b) corresponding EDS maps of Ir (cyan) and Rh (red) clearly indicating that both Ir and Rh are present in the particles. Colocation of Pt was observed, as it is part of the nanosphere template. To unambiguously demonstrate that both, Ir and Rh, are present in the small nanospheres, the extracted EDS spectrum from the lower left particle (red square in b)) is shown in (c). Similar analysis of larger particles, likely formed by cluster forming of the nanospheres, are displayed in the SI and also show both Rh and Ir.

products and possible subsequent hydrogenation products led to a mixture of products as indicated by the GC-MS analysis.

To evaluate the role of basic amines on the condensation reactions of the products, the aldehyde-bearing substrate (**7**) and product (**8**) were stirred in the presence of triethylamine (NEt_3, 5% and 10%) or *n*-butylamine (4 equiv.) under nonhydrogenative conditions (Tables S6–S7). The product compositions were evaluated by GC-MS in the presence of an internal standard after 2 h (Table S7). From the product composition, it became evident that both **7** and **8** are not significantly converted to any of the side products in the presence of catalytic quantities of base (NEt_3). In contrast, in the presence of *n*-butylamine, rapid condensation with *n*-butyl amine to the imine was observed. The latter result suggests that the conversion and loss of **7** and **8** can indeed be connected to the solvent hydrogenation products that are formed under hydrogenation conditions in the presence of Rh nanoparticles.

The mass balance loss in relation to the catalyst composition was further evaluated, by dividing the quantity of lost material (mmol) by the amount of Rh (mmol) present in the reaction mixture and plotting these as a function of the Rh:Ir ratio (expressed as x equivalents of Ir/Rh with respect to the sphere) (Figure 5). By plotting the results in this manner, it becomes evident that the mass balance loss in the presence of the postmixed nanoparticles (**Postmix @ G-sphere**) is directly correlated with the amount of rhodium nanoparticle present as this is constant around 50 mmol/mmol Rh. In contrast, in the presence of the preorganized mixed nanoparticles (**Premix @ G-sphere**), this loss in mass balance per mmol rhodium decreases with the

Rh:Ir ratio in the particle indicating a distinct change in reactivity as a result of metal mixing. These results demonstrate that catalyst preorganization indeed leads to unique catalytic behavior and suggest this strategy can effectively result in alloyed nanoparticles.

Overall, it can be seen that an optimum is reached at 16 equiv. of Ir, at which point the particles no longer display significant amine-related mass balance loss (Figure 5), whereas catalytic conversion of **7** is enhanced in the presence of Rh compared to pure Ir (Figure 4e) These results combined demonstrate that selectivity can indeed be effectively tuned to minimize solvent activation through alloying.

The formation of nanoalloys was further evidenced by energy dispersive X-ray spectroscopy (EDS) in combination with high-angle annular dark-field scanning transmission electron microscopy (HAADF-STEM) imaging (Figure 6). 2-D mapping of the encapsulated 1:1 (Rh:Ir) nanoparticles (Premix @ G-sphere*) clearly indicate homogenous distribution of Rh and Ir within even the smallest nanoparticles. In line with the TEM results (see also Figure 3), some larger particles were observed as well, possibly by clustering of the nanospheres, and analysis of these also indicate formation of rhodium–iridium alloys as Ir and Rh signals overlap (see Supporting Information, Figures S37–S39).

3. Conclusion

To summarize, we established that up to 24 sulfonate functionalized Rh metal complexes (**Rh-s**) can be encapsulated within a guanidinium functionalized nanosphere (**G-sphere**). The binding behavior was found to be akin to the related Ir^{I} complex (**Ir-s**[37]), illustrating the broader applicability of this method to other metals. Hydrogenation of the encapsulated Rh complexes led to the formation of small nanoparticles, whereas the nonencapsulated systems led to larger aggregates. The formed Rh particles were found to facilitate hydrogenation of the solvent medium and the resulting products led to compatibility issues with the sphere as well as by-product formation by follow-up reactions.

To limit this undesired activity, we investigated if the selectivity of these Rh catalysts could be tuned by preparing alloyed particles with a metal which is not active in this solvent reduction side reaction (**Ir-s**). It was demonstrated that solvent hydrogenation could effectively be suppressed when mixed Rh:Ir particles were prepared in the presence of > 66% Ir. Compared to the monometallic Ir particles (**Ir-s @ G-sphere***), the mixed Rh:Ir particles displayed higher catalytic activity in the hydrogenation of cinnamaldehyde (**7**), reaching an optimum for selectivity and activity at an 8:16 – Rh:Ir ratio. Importantly, the catalytic results illustrate that preorganization effectively facilitates the formation

of Rh:Ir alloyed nanoparticles and that the catalyst can be tuned to create an overall more active and selective catalyst compared to the monometallic or nonencapsulated Rh/Ir particles.

To conclude, the guanidinium functionalized nanosphere allows the preorganization of rhodium and iridium complexes at different ratio's, which after reduction lead to controlled formation of small alloyed Rh:Ir nanoparticles. The reactivity depends of the relative ratio of these metals. We envision that the herein developed system can be expanded to other metal catalysts and could become a powerful tool for the controlled preparation of alloys with a wider variety of metals.

Supporting Information

General procedures, detailed synthetic procedures, and additional data are available within the Supporting Information. The authors have cited additional references within the Supporting Information.

Acknowledgements

This work is part of the Advanced Research Center for Chemical Building Blocks, ARC CBBC, which is cofounded and cofinanced by The Netherlands Organization for Scientific Research and The Netherlands Ministry of Economic Affairs and Climate. Ed Zuidinga is acknowledged for his assistance with HR-MS analysis.

Conflict of Interests

The authors declare no conflict of interest.

Data Availability Statement

The data that support the findings of this study are available in the Supporting Information of this article.

Keywords: Alloy · Hydrogenation · Nanoparticles · Rhodium · Supramolecular cages

[1] M. Guerrero, N. T. Than Chau, S. Noel, A. Denicourt-Nowicki, F. Hapiot, A. Roucoux, E. Monflier, K. Philippot, *Curr. Org. Chem.* **2013**, *17*, 364–399.
[2] A. Serrano-Maldonado, S. S. Rozenel, J. L. Jimenez-Santiago, I. Guerrero-Ríos, E. Martin, *Catal. Sci. Technol.* **2018**, *8*, 4373–4382.
[3] S. Xie, X. Y. Liu, Y. Xia, *Nano Res.* **2015**, *8*, 82–96.
[4] T. S. Rodrigues, A. G. M. da Silva, P. H. C. Camargo, *J. Mater. Chem. A* **2019**, *7*, 5857–5874.
[5] B. Roldan Cuenya, F. Behafarid, *Surf. Sci. Rep.* **2015**, *70*, 135–187.
[6] R. Jin, *Nanotechnol. Rev.* **2012**, *1*, 31–56.
[7] X. Hang, S. Wang, H. Pang, Q. Xu, *Chem. Sci.* **2022**, *13*, 461–468.
[8] R. Jin, C. Zeng, M. Zhou, Y. Chen, *Chem. Rev.* **2016**, *116*, 10346–10413.
[9] M. Ibrahim, R. Poreddy, K. Philippot, A. Riisager, E. J. Garcia-Suarez, *Dalt. Trans.* **2016**, *45*, 19368–19373.
[10] M. Ibrahim, M. A. S. Garcia, L. L. R. Vono, M. Guerrero, P. Lecante, L. M. Rossi, K. Philippot, *Dalt. Trans.* **2016**, *45*, 17782–17791.
[11] L. Xu, D. Liu, D. Chen, H. Liu, J. Yang, *Heliyon* **2019**, *5*, e01165.
[12] O. Wetzel, O. Prymak, K. Loza, N. Gumbiowski, M. Heggen, P. Bayer, C. Beuck, C. Weidenthaler, M. Epple, *Inorg. Chem.* **2022**, *61*, 5133–5147.
[13] M. Boutonnet, J. Kizling, P. Stenius, G. Maire, *Colloids Surf.* **1982**, *5*, 209–225.
[14] I. Nakamula, Y. Yamanoi, T. Yonezawa, T. Imaoka, K. Yamamoto, H. Nishihara, *Chem. Commun.* **2008**, 5716–5718.
[15] T. Tsukamoto, K. Tomozawa, T. Moriai, N. Yoshida, T. Kambe, K. Yamamoto, *Angew. Chemie Int.* **2022**, *61*, e202114353.
[16] I. Nakamula, Y. Yamanoi, T. Imaoka, K. Yamamoto, H. Nishihara, *Angew. Chemie – Int. Ed.* **2011**, *50*, 5830–5833.
[17] X. Li, C. Zhang, M. Luo, Q. Yao, Z. H. Lu, *Inorg. Chem. Front.* **2020**, *7*, 1298–1306.
[18] J. K. Sun, W. W. Zhan, T. Akita, Q. Xu, *J. Am. Chem. Soc.* **2015**, *137*, 7063–7066.
[19] L. Zhu, S. Zhang, X.-C. Yang, Q. Zhuang, J.-K. Sun, *Small Methods* **2022**, *6*, 2200591.
[20] I. E. Ertas, M. Gulcan, A. Bulut, M. Yurderi, M. Zahmakiran, *J. Mol. Catal. A Chem.* **2015**, *410*, 209–220.
[21] T. Huang, G. Sheng, P. Manchanda, A. H. Emwas, Z. Lai, S. P. Nunes, K.-V. Peinemann, *Sci. Adv.* **2023**, *5*, eaax6976.
[22] X. Yang, Q. Xu, *Trends Chem.* **2020**, *2*, 214–226.
[23] L.-M. Cao, J. Zhang, X.-F. Zhang, C.-T. He, *Chem. Sci.* **2022**, *13*, 1569–1593.
[24] J.-Y. Li, X.-D. Yang, F.-X. Chen, J.-K. Sun, *Mater. Chem. Front.* **2023**, *7*, 5355–5376.
[25] C. Wang, F. Sun, G. He, H. Zhao, L. Tian, Y. Cheng, G. Li, *Curr. Opin. Colloid Interface Sci.* **2023**, *63*, 101660.
[26] V. T. Liveri, *Control Synthesis of Nanoparticles in Microheterogeneous Systems*, Springer, New York, NY **2006**.
[27] L. Qiu, R. McCaffrey, W. Zhang, *Chem. – An Asian J.* **2018**, *13*, 362–372.
[28] S. Sato, J. Iida, K. Suzuki, M. Kawano, T. Ozeki, M. Fujita, *Science* **2006**, *313*, 1273–1276.
[29] K. Harris, D. Fujita, M. Fujita, *Chem. Commun.* **2013**, *49*, 6703–6712.
[30] K. Harris, Q.-F. Sun, S. Sato, M. Fujita, *J. Am. Chem. Soc.* **2013**, *135*, 12497–12499.
[31] M. Tominaga, K. Suzuki, M. Kawano, T. Kusukawa, T. Ozeki, S. Sakamoto, K. Yamaguchi, M. Fujita, *Angew. Chem., Int. Ed.* **2004**, *43*, 5621–5625.
[32] J. Liu, T. Luo, Y. Xue, L. Mao, P. J. Stang, M. Wang, *Angew. Chemie* **2021**, *133*, 5489–5495.
[33] X. Yan, P. Wei, Y. Liu, M. Wang, C. Chen, J. Zhao, G. Li, M. L. Saha, Z. Zhou, Z. An, X. Li, P. J. Stang, *J. Am. Chem. Soc.* **2019**, *141*, 9673–9679.
[34] Q. Q. Wang, S. Gonell, S. H. A. M. Leenders, M. Dürr, I. Ivanovic-Burmazovic, J. N. H. Reek, *Nat. Chem.* **2016**, *8*, 225–230.
[35] F. Yu, D. Poole, S. Mathew, N. Yan, J. Hessels, N. Orth, I. Ivanović-Burmazović, J. N. H. Reek, *Angew. Chemie – Int. Ed.* **2018**, *57*, 11247–11251.
[36] S. Gonell, J. N. H. Reek, *ChemCatChem* **2019**, *11*, 1458–1464.
[37] L. Metz, E. Bobylev, K. Brouwer, A. van Blaaderen, R. van de Poll, V. Drozhzhin, E. Hensen, J. Reek, *Chem. Sci.* **2024**, *15*, 20022–20029
[38] B. L. Tran, J. L. Fulton, J. C. Linehan, J. A. Lercher, R. M. Bullock, *ACS Catal.* **2018**, *8*, 8441–8449.
[39] W. Oberhauser, C. Evangelisti, A. Liscio, A. Kovtun, Y. Cao, F. Vizza, *J. Catal.* **2018**, *368*, 298–305.
[40] C. Cerezo-Navarrete, P. Lara, L. M. Martínez-Prieto, *Catalysts* **2020**, *10*, 1144.
[41] Q. Q. Wang, S. Gonell, S. H. A. M. Leenders, M. Dürr, I. Ivanovic-Burmazovic, J. N. H. Reek, *Nat. Chem.* **2016**, *8*, 225–230.
[42] M. A. N. Virboul, *Sulfonate Functionalisation of Transition Metal Complexes: A Versatile Tool Towards Catalyst Recovery*, Utrecht University, Utrecht **2011**.
[43] C. Gütz, R. Hovorka, C. Klein, Q. Q. Jiang, C. Bannwarth, M. Engeser, C. Schmuck, W. Assenmacher, W. Mader, F. Topic¨, K. Rissanen, S. Grimme, A. Lützen, *Angew. Chemie – Int. Ed.* **2014**, *53*, 1693–1698.
[44] Y. Monguchi, M. Mizuno, T. Ichikawa, Y. Fujita, E. Murakami, T. Hattori, T. Maegawa, Y. Sawama, H. Sajiki, *J. Org. Chem.* **2017**, *82* 10939–10944.
[45] H. Sajiki, T. Ikawa, K. Hirota, *Org. Lett.* **2004**, *6*, 4977–4980.
[46] M. Sun, L. Wei, C. Li, *J. Am. Chem. Soc.* **2023**, *145*, 3897–3902.

Manuscript received: July 01, 2024
Revised manuscript received: November 11, 2024
Accepted manuscript online: December 02, 2024
Version of record online: ■■, ■■